Nano storage-boxes constructed by the vertical growth of MoS2 on graphene for high-performance Li-S batteries

Nano storage-boxes constructed by the vertical growth of MoS_2 on graphene for high-performance Li-S batteries

Bowen Cui[a, 1], Xiaomin Cai[a,1], Wenqiang Wang[a], Petr Saha[b], Gengchao Wang[a,*]

[a]*Shanghai Key Laboratory of Advanced Polymeric Materials, Shanghai Engineering Research Center of Hierarchical Nanomaterials, School of Materials Science and Engineering, East China University of Science and Technology, Shanghai 200237, China*

[b]*Centre of Polymer Systems, University Institute, Tomas Bata University, Tr. T. Bati 5678, Zlin 76001, Zlín, Czech Republic*

[*]*Corresponding author. E-mail address: gengchaow@ecust.edu.cn (G. Wang).*

ABSTRACT

In order to accelerate the reaction kinetics of lithium-sulfur batteries, the introduction of electro catalysis and proper structural control of the sulfur cathode is urgently needed. MoS_2 nano sheets was selectively grown vertically (V-MoS_2) on the microwave-reduced graphene (rGO) sheets through chemical coupling to construct a self-supporting sulfur cathode with a nano storage-box structure (V-MoS_2 as the wall and rGO as the bottom). RGO, which has a high conductivity of 37 S cm^{-1}, greatly accelerates the transfer of electrons from the active sites on the edge of the layer to the solution. The introduction of carbon tubes can connect the abundant pores in the foam and act as a long-range conductive path. The 2D-orthogonal-2D structure maximally exposes the edge active sites of MoS_2, and together with graphene form a nano reactor of sulfur, intermediate lithium polysulfides and discharge product $Li_2S_{(2)}$. The effective combination of the microstructure confinement of the nano storage-boxes and the efficient synchronous catalytic mechanism of V-MoS_2 greatly improves the electrochemical performance of the lithium-sulfur batteries. As a result, the assembled lithium-sulfur battery displays a high initial discharge capacity of 1379 mAh g^{-1}, good cycle stability (86% capacity retention after 500 cycles at 0.1C) and superior rate performance. © 2021 Science Press and Dalian Institute of Chemical Physics, Chinese Academy of Sciences. Published.

Keywords: Edge-rich MoS_2, nano boxes, catalytic conversion, lithium-sulfur batteries

1. Introduction

The multi-electron reaction of light elements is the development direction of future batteries [**1-3**]. The sulfur reduction process of 16 electrons in lithium-sulfur batteries fits this point, which is very meaningful for the development of high energy density devices [**4-8**]. However, the reaction process is troubled by slow sulfur reduction kinetics **[9]** and polysulfide shuttle effect [**10**]. There are endless researches on sulfur cathodes [**11-14**]. From the analysis of the internal reaction, the initial cleavage of the S8 ring molecule is a relatively easy process, and the subsequent cleavage into shorter chain polysulfide molecules becomes more and more difficult [**15,16**]. The reaction rate of the sulfur cathode is 10^{-6} A cm^{-2}, which is four orders of magnitude slower than that of the lithium anode [**17,18**]. It can

be seen that the sulfur cathode is a rate control step [**19,20**]. In addition, researchers have made considerable efforts to solve the shuttle effect of lithium polysulfides (LiPSs), but passive restriction or retention strategies cannot fundamentally prevent the dissolution of polysulfide into the electrolyte. Therefore, it is urgent to introduce effective electro catalytic means and adjust the structure of sulfur cathode [**21-23**].

In recent years, a series of polar hosts such as metal oxides [**21,24**], metal sulfides [**25,26**], metal carbides [**17,27,28**], metal nitrides [**29,30**], metal phosphides [**31-33**] and metal-free hosts [**34-36**] have been found to have catalytic activity for the conversion of LiPSs. Compared with other materials, metal sulfides [**37**] have superior catalytic activity in promoting the redox reaction kinetics of LiPSs, thanks to the metal-S bond that can anchor lithium polysulfide through dipole interaction [**38-40**]. The twodimensional (2D) layered structure of molybdenum disulfide (MoS_2) has high electrochemical activity due to the presence of sulfur vacancies, which has attracted widespread attention [**4143**]. However, in the normal MoS_2 material, only the edge sites are the active regions with catalytic activity, while the planar regions are catalytically inactive [**44**]. The existing improvement methods can be roughly divided into two categories. One is to generate and expose as many active edge sites as possible through the design of nanostructures [**45**], that is, to increase the proportion of edge sites. Another method is to change the nature of the inert planar region to convert it into an active region [**46**]. Obviously, the nano crystallization of MoS_2 is a simpler and more effective way to improve electro catalytic performance [**47,48**]. However, nanoscale MoS2 is easy to agglomerate, and it is possible to synthesize a layered nano-catalyst with abundant edge sites by using some conductive materials as the substrate [**49-51**].

Graphene has a unique electronic structure [**52**]. Each carbon atom in its two-dimensional plane has three *"p"* orbitals and one *"s"* orbital. The excellent conductivity of graphene is derived from the remaining *p* electrons on the *"p"* orbital [**53,54**]. Graphene has become an excellent candidate for the electro catalyst carrier due to its high conductivity and large specific surface area [**55,56**]. Li et al. [**57**] used graphene with CoS_2 particles uniformly grown on both sides as the sulfur carrier, and successfully promoted the conversion of Li_2S_6 and Li_2S_2/Li_2S in the liquid electrolyte.

Herein, we used simple hydrothermal to make MoS_2 selectively grow vertically on the graphene sheets reduced by microwave through chemical coupling, and prepared a self-supporting sulfur cathode with high catalytic activity. After the graphene foam is immersed in the carbon nanotube solution, the carbon tubes can connect to the abundant pores in the foam and play a long-range conductive role. This interconnected three-dimensional carbon conductive network is very beneficial to the transfer of electrons and ions. The microwave-reduced graphene foam has excellent electronic conductivity (close to 40 S cm^{-1}), which greatly accelerates the transfer of electrons from the active sites on the edge of the layer to the solution. The 2D-orthogonal-2D structure maximally exposes the edge active sites of V-MoS_2, and together with the conductive substrate graphene sheet, forms a nano-storage box of sulfur, intermediate LiPSs and $Li_2S_{(2)}$. The effective combination of structural confinement and chemical catalysis greatly improves the electrochemical performance of the battery. The results show that the V-MoS_2/rGOCTF@S//LE//Li lithium-sulfur battery exhibits a high degree of reversibility, and the first discharge capacity reaches 1379 mAh g^{-1}. The average capacity decay per cycle during 500 cycles is only 0.028%.

2. Experimental

2.1. Preparation

2.1.1. Preparation ofrGO and rGOCTF

The graphene oxide solution (solid content about 5 mg mL^{-1}) and the carboxylated carbon nanotube solution (solid content about 5 mg mL^{-1}) were prepared by modified Hummers [**58**] and mixed acid treatment methods [**59**], respectively. Firstly, use a straw to transfer the graphene oxide solution to a cylindrical container and freeze-dried for twelve hours to form a graphene oxide foam. Secondly, put the foam in a round-bottomed flask and vacuum for 5 min to remove air, and reduced graphene oxide foam (rGO foam) was obtained by microwave for 20 s afterward. Then, put the rGO foam in the carboxylated carbon nanotube solution, and finally get reduced graphene oxide/carbon nanotubes foam (rGOCTF) after the same process as above.

2.1.2. Preparation of V-MoS_2/rGOCTF composites

First, 0.3 g $NaMoO_4$, 0.3 g thiourea (CH_4N_2S), and 0.48 g sodium oleate ($C_{17}H_{33}CO_2Na$) were dissolved in a 20 mL mixture of deionized water and absolute ethanol ($v/v = 1:1$), then stirred for 1 h and ultrasonic for 5 min to obtain a uniform solution. The rGOCTF was immersed in the precursor solution, and vacuum filtration is used to remove the gas in the foam by vacuum filtration so that the precursor solution can completely enter the foam. It is then transferred into a 50 mL Teflon-lined stainless-steel autoclave, heated in an oven to 200 °C for 12 h, and cooled naturally to room temperature after the reaction. The above samples were washed with absolute alcohol and deionized water several times, and then V-MoS_2/rGOCTF foam was obtained after freeze-drying.

2.1.3. Polysulfide adsorption test and kinetics study

2 mmol L^{-1} Li_2S_6 was synthesized by adding S and Li_2S with a molar ratio of 5:1 in dimethoxyethane (DME) under vigorously stirring at 50 °C. A corresponding amount (20 mg) of rGO foams, V-MoS_2/rGOCTFs were added into 5 mL of the as-prepared Li_2S_6 solution, respectively. Then optical images were compared to show the difference in adsorption capability after standing for 2 h.

For symmetric cells, the electrolyte containing about 0.5 mol L^{-1} Li_2S_6 and 1 mol L^{-1} LiTFSI was prepared in DME and 1,3-Dioxolane (DOL) ($1:1, V:V$) solution. The obtained catalysts electrodes were used as identical working and counter electrodes. Cyclic voltammetry (CV) measurements of these symmetric cells were conducted between - 0.8 and 0.8 V at a scan rate of 1 mV s^{-1}. For Li_2S nucleation tests, 0.3 mol L^{-1} Li_2S_8 and 1 mol L^{-1} LiTFSI in tet-raglyme solution were prepared. Li foil and Celgard 2400 membranes were used as the anode and separator. Li_2S_8/tetraglyme (20 μL) is first distributed into the cathode, and then 20 pL of blank electrolyte but without Li_2S_8 is dropped onto lithium anode. The cells are galvanostatically discharged to 2.06 V under a current of 50 mA g^{-1} and are potentiostatically kept at 2.05 V until the current drops below 10^{-5} A for deposition and growth of Li_2S on various host surfaces.

2.1.4. Preparation of sulfur cathode and assembly of battery

First, dissolve the sulfur powder in carbon disulfide (S/CS_2, concentration about 100 mg mL^{-1}), and drop a certain amount of the above solution on the V-MoS_2/rGOCTF. After it is completely absorbed, vacuum filtration was performed to remove CS_2. Finally, the foam was heated slowly in an argon

atmosphere to 155 °C for 12 h. The area of cathode was 1.44 cm^2. After being cooled naturally, the free-standing sulfur cathode (V-MoS_2/rGOCTF@S) with different sulfur loading (4-6 mg cm^{-2}) was obtained.

The CR2025 coin-type cells were assembled in an argon-filled glovebox. The prepared V-MoS_2/rGOCTF@S served as a cathode, the pure lithium foil served as an anode and the microporous polypropylene (Celgard 2400) served as a separator. The electrolyte consists of 1 mol L^{-1} lithium bis-(trifluoromethyl sulfonyl) imide (LiTFSI) in a mixture of DME and DOL ($1{:}\ 1, V{:}\ V$) with 1 wt% $LiNO_3$, and the E/S ratio in each cell is $\sim$ 10 μL mg^{-1}.

2.2. Characterization

The morphologies of all samples were characterized by field emission scanning electron microscopy (FESEM, Hitachi S4800) and high-resolution transmission electron microscopy (HRTEM, JEOL JEM2100). Energy dispersive spectroscopy (EDS) elemental mapping was performed on a QUANTAX 400-30 detector on a Hitachi S4800. XRD patterns were collected on a Rigaku D/ MAX2550 VB/PC with Cu K_α radiation (λ = 1.54 Å) over the range of 5°-75° (2θ) at room temperature. X-ray photoelectron spectroscopy (XPS) measurements were performed on a Thermo Scientific K-Alpha + instrument with a monochromatic Al K_a X-ray source (1486.6 eV). Raman spectroscopy test was performed on a Renishaw inVia + Reflex with a 50 mW He-Ne laser operated at 532 nm. The specific surface area was measured by the multipoint Brunauer-Emmett-Teller (BET) method at 77 K with a Micromerit-ics ASAP2460 system. The thermogravimetric analysis (TGA, NETZSCH TG209F1-GC) was carried out from room temperature to 800 °C at a heating rate of 10 °C min^{-1} under Air or Nitrogen atmosphere.

2.3.Electrochemical measurements

The galvanostatic measurement of CR2025 was performed between 1.7 and 2.8 V for low rates (0.1C, 0.2C, 0.5C, 1.0C, 2.0C, 4.0C, 5.0C) at room temperature on a LAND-CT2001A battery system. CV measurements and electrochemical impedance spectra (EIS) testing of CR2025 were performed using a CHI 760E electrochemical workstation. The scan rate and voltage range of CV measurements were 0.1 mV s^{-1} and 1.7-2.8 V, respectively. For the EIS testing, the frequency range was from 100 kHz to 10 mHz. All the electrochemical tests were performed at ambient temperature.

3. Results and discussion

3.1. Morphology and structure

The nanometerization of MoS_2 facilitates the exposure of its active edges, but the pure nano-MoS_2 is easy to agglomerate as shown in **Fig. S1**. As shown in **Fig. S2**(a-c), a highly conductive rGO foam ($\sim$37 S cm^{-1}) was obtained by rapid microwave reduction of freeze-dried graphene foam. Due to the freeze-drying method, the pores in rGO foam belong to macro-porous structure (as shown in **Fig. S2**d and e), and the pore size distribution is about 10-20 pm. **Fig. 1**(a) vividly shows the preparation process of the V-MoS_2/rGOCTF@S cathode. The FE-SEM photo of the rGOCTF (**Fig. 1**b) shows that the carbon nanotubes with high aspect ratio are interspersed in the three-dimensional pores of the rGO foam. The addition of a small amount of CNTs will not affect the original conductive path in the system (the electronic conductivity is still maintained at 37 S cm^{-1}), and its function is to provide a long-range conductive path. Compared with **Fig. S3**(b), MoS_2 nanosheets are clearly stacked and aggregated into

a spherical shape to attach to the graphene sheet. The presence of the surfactant sodium ole-ate makes the molybdenum disulfide nanosheets vertically and uniformly distributed on the graphene layer (**Fig. S3**b). From **Fig. 1**(c-e), it can be clearly seen that MoS_2 successfully achieved vertical growth on the graphene conductive substrate. In addition, **Figs. S4-S6** study the optimal concentration of MoS_2 precursors. Finally, 3 mmol L^{-1} was selected as the optimal concentration due to its complete nano storage-boxes morphology, the ability to capture and transform lithium polysulfides equivalent to 4 mmol L^{-1}, and the small sacrifice of electronic conductivity. The element content curve (**Fig. S7**) corresponding to **Fig. 1**c proves the existence of V-MoS_2. Interestingly, these layers are overlapped to form several small nano storage-boxes (about 50 x 50 nm^2 in size) with V-MoS_2 as the wall and rGO as the bottom. According to the analysis of Fig. 1f and **Fig. S8**, the interlayer spacing of the V-MoS_2 is 0.63 nm. Unlike the random agglomeration loading of sulfur on the rGOCTF@S (**Fig. S9**), the V-MoS_2/rGOCTF@S perfectly encapsulates sulfur particles uniformly in the nano storage-boxes (**Fig. 1**g and **Fig. S10**).

The XRD patterns of rGO, MoS_2, and V-MoS_2/rGOCTF were shown in **Fig. 2**(a). The absence of a peak near 10° in the rGO indicates that graphene oxide is highly reduced, and the broad diffraction peak at the range of 20°-30° corresponds to its (002) crystal plane. The characteristic peaks at 14.4°, 33.5°, and 58.3° in the V-MoS_2/rGOCTF correspond to the (002), (100), and (110) crystal planes of MoS_2, respectively, proving the successful growth of MoS_2. In the Raman spectra (**Fig. 2**b), the peaks at 378 and 404 cm^{-1} correspond to the E_{2g} in-plane and A_{1g} out-of-plane bending vibrations of V-MoS_2, respectively [**60**]. Compared with the commercial MoS_2, E_{2g} and A_{1g} of the V-MoS_2 have a red shift, indicating that the lattice parameters along the C axis have changed, and the thickness of the V-MoS_2 layer has been reduced [**61**]. In addition, the peak intensity of out-of-plane vibration is sig- nificantly higher than that of in-plane vibration, proving that more edge active sites of the V-MoS_2 are exposed [**62,63**]. In the V-MoS_2/ rGOCTF, the peak intensity ratio of D-band and G-band (ID/IG) of graphene increases significantly, indicating that the defect density of the composite increases. The graphene and V-MoS_2 nano sheets overlap each other to form a three-dimensional network structure with abundant pores. Such a porous structure facilitates ion transport and provides a large number of active sites for the reaction. From the BET result (**Fig. 2**c), it is a typical type IV gas adsorption and desorption isotherm, and its pore size distribution is mainly concentrated around 17 nm, which is a typical mesoporous material. More importantly, the hysteresis ring belongs to the H3 type, which means that its pore structure is a kind of slit-like holes formed by flaky particles [**64**], which corresponds to the nano storage-boxes morphology seen in TEM and FE-SEM images. The composite macro-porous structure of rGOCTF (**Fig. S2**d) and meso-porous of V-MoS_2/rGOCTF not only makes the loading of sulfur more uniform, but also makes the electrolyte easy to be impregnated, which is conducive to the electrochemical reaction. The atomic ratio of Mo to S in the XPS spectrum (**Fig. 2**d) is 6.06:13.5, which is close to 1:2. In **Fig. 2**(e), the characteristic peaks of binding energy at 232.3 and 228.3 eV correspond to Mo $3d_{3/2}$ and $3d_{5/2}$ orbitals in V-MoS_2. The small peak with a binding energy of 235.6 eV is assigned to Mo^{6+} $3d_{3/2}$, which may be due to the replacement of sulfur in MoS_2 by oxygen in GO during the heat treatment to form MoO_3 [**65**]. The peak at 226.2 eV corresponds to the S 2s orbital, because it is easy to coincide with the Mo 3d orbital. In **Fig. 2**(f), the characteristic peaks of binding energy at 162.1 and 163.3 eV correspond to the S $2p_{3/2}$ and $2p_{1/2}$ orbitals in MoS_2, respectively.

3.2. Adsorption-catalytic-conversion performances

The static adsorption experiment in **Fig. 3**(a and b) shows the chemical capture of Li2S6 by different samples. It can be clearly seen that the color of the solution in the V-MoS_2/rGOCTF fad to almost colorless after 3 h compared with the rGOCTF and the original Li_2S_6 solution. This phenomenon

confirms that V-MoS_2/ rGOCTF can effectively anchor LiPSs and inhibit the ‘‘shuttle effect”. In addition, ultraviolet-visible (UV-vis) absorption spectroscopy (**Fig. 3**c) analyzed the supernatants of the three bottles after adsorption. All samples showed a wide absorption region from 250 to 300 nm, and the peak near 260 nm could be attributed to S^{2-}_6 species. The decrease of the peak intensity of V-MoS_2/rGOCTF indicates that it can capture LiPSs more effectively. The XPS spectra after adsorption of Li_2S_6 (**Fig. 3**d) shows that the binding energy of Mo 3d orbital is about 0.2-0.3 eV lower than before adsorption, while the binding energy of S 2p orbital shifts to the direction of higher binding energy. This shows that the transfer of electron occurs between V-MoS_2/rGOCTF and LiPSs, and there is a strong chemical interaction [**66**].

In order to further explore the LiPSs conversion ability of V-MoS_2/rGOCTF, Li_2S deposition experiments were carried out on the surface of rGOCTF and V-MoS_2/rGOCTF. Perform nonlinear fitting on the potentiostatic discharge curves (**Fig. 3**e and f). The purple area represents the reduction of Li_2S_8, the gray part represents the reduction of Li_2S_6, and the rest is the precipitation of Li_2S. According to Faraday’s law, the amount of charge is used to evaluate the ability of Li_2S conversion [**38**]. Obviously, the capacity of Li_2S precipitated on V-MoS_2/rGOCTF (143.3 mAh g^{-1}) is much higher than that of rGOCTF (77.2 mAh g^{-1}). These results clearly show that V-MoS_2/rGOCTF greatly promotes the rapid conversion to Li_2S.

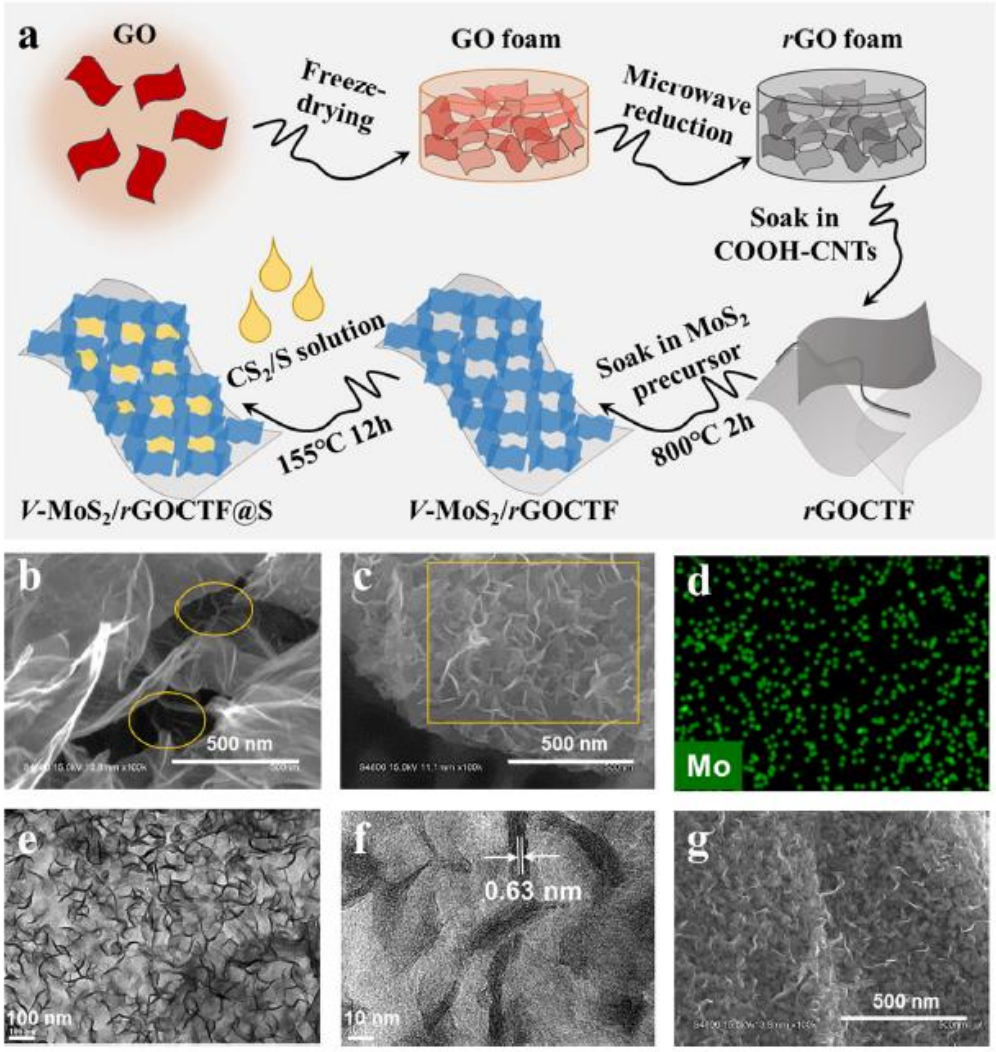

Fig. 1. (a) Schematic illustration of the formation of V-MoS_2/rGOCTF@S. FE-SEM images of (b) rGOCTF, (c) V-MoS_2/rGOCTF with precursor concentration of 3 mmol L^{-1} and (d) corresponding surface scanning EDS of Mo. (e) TEM and (f) HRTEM images of V-MoS_2/rGOCTF. (g) FE-SEM image of V-MoS_2/rGOCTF@S.

3.3. Electrochemical performance

The symmetrical cells without (**Fig. S11**) and with (**Fig. 4**a) Li_2S_6 were further assembled, and the CV tests were performed at a scan rate of 1 mV s^{-1} in the potential region of + 0.8 to - 0.8 V. The CV without Li_2S_6 electrolyte is used to correct the capacitance contribution, and the capacitance/current it provides can be ignored. The CV curve of V-MoS_2/rGOCTF shows two obvious reduction peaks at 0.028 and - 0.37 V, and two oxidation peaks at - 0.028 and 0.37 V, indicating the redox reaction of LiPSs on the V-MoS_2/rGOCTF electrode has a high degree of reversibility. Since Li_2S_6 is the only electrochemically active substance in symmetrical cell, the peaks at 0.026 and - 0.37 V in cathodic scan are attributed to the reduction from Li2Sn ($6 < n \leq 8$) to Li_2S_6 and the reduction from Li_2S_6 to Li_2S (Li_2S_2), and the peaks at - 0.028 and 0.37 V in anodic scan are attributed to the oxidation from Li_2S (Li_2S_2) to Li_2S_6 and the oxidation from Li_2S_6 to Li_2Sn ($6 < n \leq 8$). For the rGOCTF electrode, only a pair of very broad redox peaks is detected, which means the reduction of Li_2S_6 on the rGOCTF is slow and the above progress could not be distinguished.

In order to evaluate the electrocatalytic effect of V-MoS_2/ rGOCTF@S on lithium-sulfur batteries, we compared the Nyquist plots (**Fig. 4**b) and CV curves (**Fig. 4**c) of rGOCTF//LE//Li and V-MoS_2/rGOCTF@S//LE//Li cells. The sulfur contents of rGOCTF@S and V-MoS_2/rGOCTF@S measured by the TG curves (**Fig. S12**a) are 76.8% and 79.1%, respectively, and the average sulfur loading is 5.6 mg cm^{-2}, and the V-MoS_2 contents of V-MoS_2/rGOCTF@S is 31.2 wt% (**Fig. S12**b). The body resistance (Rb) changes before and after loading V-MoS_2 are very small (1.89 and 2.14 X), indicating that the introduction of V-MoS_2 has little effect on the conductivity of the electrode, which corresponds to the result in **Fig. S6**.

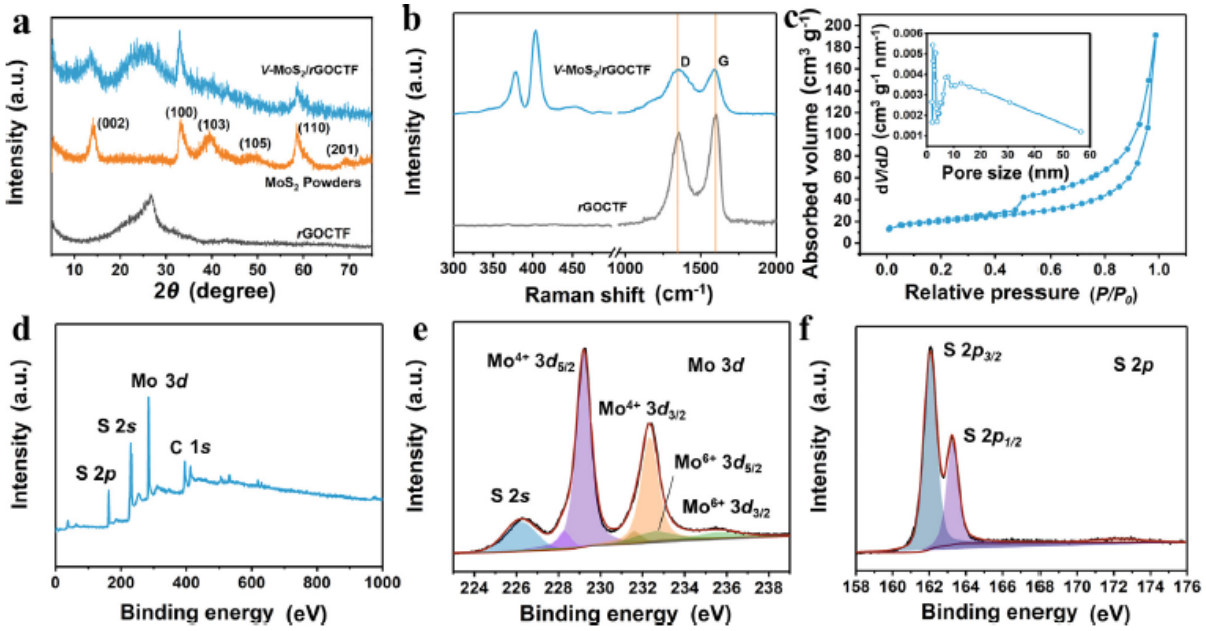

Fig. 2. (a) XRD patterns and (b) Raman spectra of rGOCTF and V-MoS_2/rGOCTF. (c) N_2 adsorption/desorption isotherm and pore size distribution curve (inset) of the V-M0S_2/ rGOCTF. (d) XPS survey spectrum, (e) Mo 3d XPS spectrum and (f) S 2p XPS spectrum of V-MoS_2/rGOCTF.

However, the Li+ charge transfer resistance (Rct) at the electrode-electrolyte interface of the V-MoS_2/rGOCTF@S//LE//Li cell is significantly lower than that of the rGOCTF@S//LE//Li cell, which is conducive to the rapid progress of the redox reaction. It can be seen from the CV curves (**Fig. 4**c and **Fig. S13**) that the reduction peak between 2.2-2.4 V corresponds to the conversion of elemental sulfur to higher-order lithium polysulfides, and the reduction peak at 1.9-2.1 V corresponds to the continuous

conversion to lower-order lithium sulfide. Compared with the rGOCTF@S//LE//Li and MoS_2/rGOCTF@S//LE//Li cells, the V-MoS_2/rGOCTF@S//LE//Li cell has higher redox peak currents. In addition, the reduction peaks of V-MoS_2/rGOCTF@S//LE//Li cell shift to the high voltage direction, and the oxidation peak shifts to the low voltage direction, which indicates that the reaction kinetics and reversibility are greatly enhanced.

Fig. 4(d) is a zoom enlarged view of the CV curves in the voltage range from 2.005 to 2.065 V to describe the onset reduction proces of sulfur. It was found that the V-MoS_2/rGOCTF shifted to the high potential direction, indicating that the reduction reaction started earlier and the required start reaction potential was lower. According to the Tafel equation, the over potential has a linear relationship to the log *i*. Do the Tafel curves (**Fig. 4**e) for the voltage range framed in the box of **Fig. 4**(d), and find that the slope of the V-MoS_2/rGOCTF (40 mV dec^{-1}) is much lower than that of the rGOCTF (77 mV dec^{-1}), indicating that within the same voltage range, the current range of the V-MoS_2/rGOCTF is larger. That is to say, there are more substances involved in the redox reaction, and the acceleration rate of the redox reaction is faster.

In the charge-discharge curve at 0.1C (**Fig. 4**f), compared with the rGOCTF@S//LE//Li (322 mV), the V-MoS_2/rGOCTF@S//LE//Li cell has smaller over potential (158 mV), which is consistent with the CV results. In addition to kinetic reversibility, the V-MoS_2/ rGOCTF@S//LE//Li cell also has good rate performance (**Fig. 4**g). At 0.1C, the initial discharge capacity reached 1379 mAh g^{-1}. When the current density is as high as 5C, the discharge capacity is still 530 mAh g^{-1}. While the current density returns to 0.1C, it still has a specific capacity of 1210 mAh g^{-1}. However, at 0.1C, the first cycle discharge capacity of the rGOCTF@S//LE//Li cell is 981 mAh g^{-1}. When the current density reaches 5C, the discharge capacity is only 260 mAh g^{-1}. Futhermore, **Fig. 4**(h) shows the cycling performance of different batteries. After 500 cycles, the discharge capacity of the rGOCTF@S//LE//Li is 503 mAh g^{-1}, and the capacity retention rate is 51%.

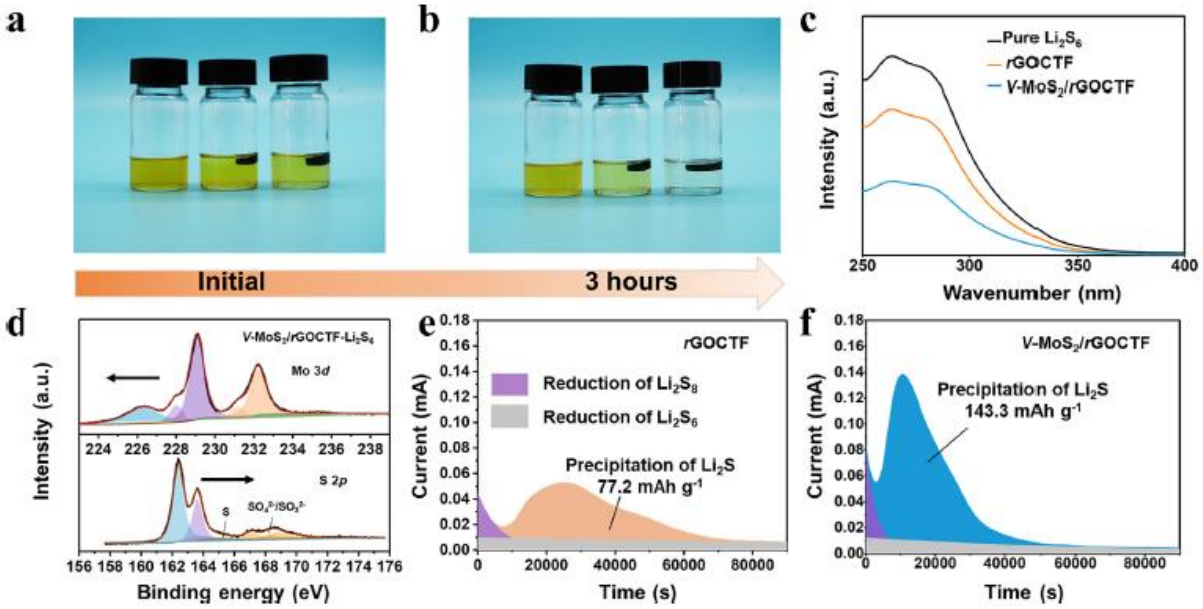

Fig. 3. Photos of different samples soaked in a Li_2S_6/DOL/DME solution (a) initial state and (b) after 3 h. (c) UV-vis spectra of the solution after static adsorption of Li_2S_6. (d) XPS spectra show Mo 3d and S 2p of V-MoS_2/rGOCTF after soaked in a Li_2S_6/DOL/DME solution. Potentiostatic discharge curves of Li_2S_8/tetraglyme solution at 2.05 V on (e) rGOCTF and (f) V-MoS_2/rGOCTF surfaces.

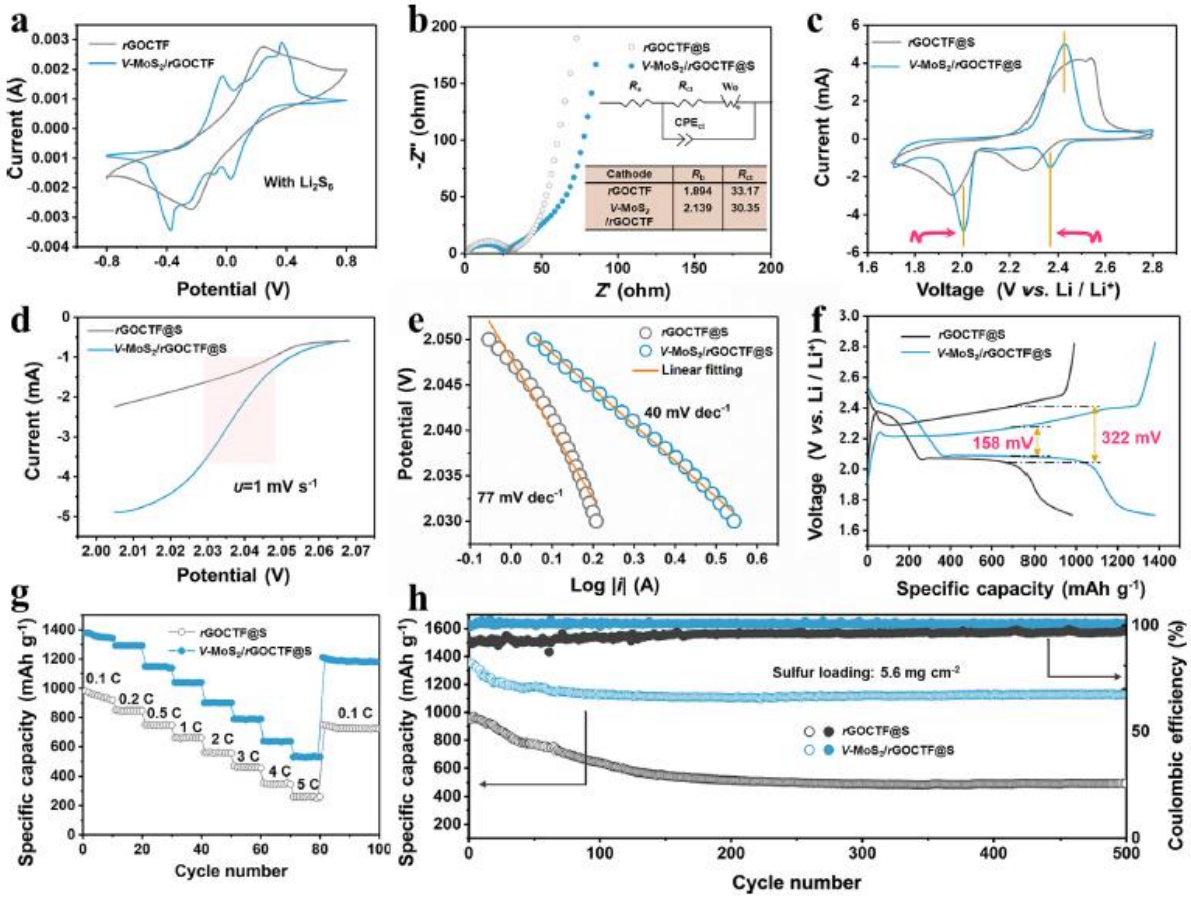

Fig. 4. CV curves of symmetric cells with Li_2S_6 using rGOCTF and V-MoS_2/rGOCTF as working electrodes. (b) Nyquist plots and (c) CV curves recorded in the range of 1.7 to 2.8 V at a scan rate of 0.1 mV s^{-1} of rGOCTF@S//LE//Li and V-MoS_2/rGOCTF@S//LE//Li cells. (d) Zoomed image of CV recorded on rGOCTF and V-MoS2/rGOCTF electrodes at a scan rate of 1 mV s^{-1} and (e) corresponding Tafel plots. (f) Charge/discharge profiles, (g) rate performance, and (h) cycling performance of rGOCTF@S//LE//Li and V-MoS_2/ rGOCTF@S//LE//Li cells.

After 500 cycles, the discharge capacity of the V-MoS_2/rGOCTF@S//LE//Li can still reach 1190 mAh g^{-1}, the capacity retention rate is 86%, and the average capacity attenuation per cycle is only 0.028%. In order to evaluate the influence of the vertical growth of MoS_2 on the cycle life of the battery, **Fig. S14** compares the 200 cycles stability of common MoS_2 and V-MoS_2 at a high current density of 1C. After 200 cycles, the discharge capacity of the V-MoS_2/rGOCTF@S//LE//Li can still reach 847 mAh g^{-1} which is much higher than that of V-MoS_2/rGOCTF@S//LE//Li (336 mAh g^{-1}). In addition, it can be seen in **Fig. S15** that even under high sulfur load (> 5 mg cm^{-2}) and high current density 1C, the cycling life of V-MoS_2/rGOCTF@S//LE//Li is significantly better than rGOCTF@ S//LE//Li battery. All of these indicate that the vertical arrangement of molybdenum disulfide nanoarrays has better stability and activation effect on the active substances in the process of continuous morphological transformation.

3.4. Electro catalytic mechanism

Unlike the bulk agglomeration of active materials on rGOCTF and the weak interaction between pure carbon materials and LiPSs (**Fig. S16**), the nano storage-boxs structure formed by the vertical growth of MoS_2 on the graphene sheet in the V-MoS_2/rGOCTF@S effectively promotes the uniform dispersion of the active materials (**Fig. 5**a). Each nano storage-box is like a nano-reactor, which ensures the high-

speed and orderly progress of the redox reaction. The 2D-orthogonal-2D structure can expose more edge active sites.

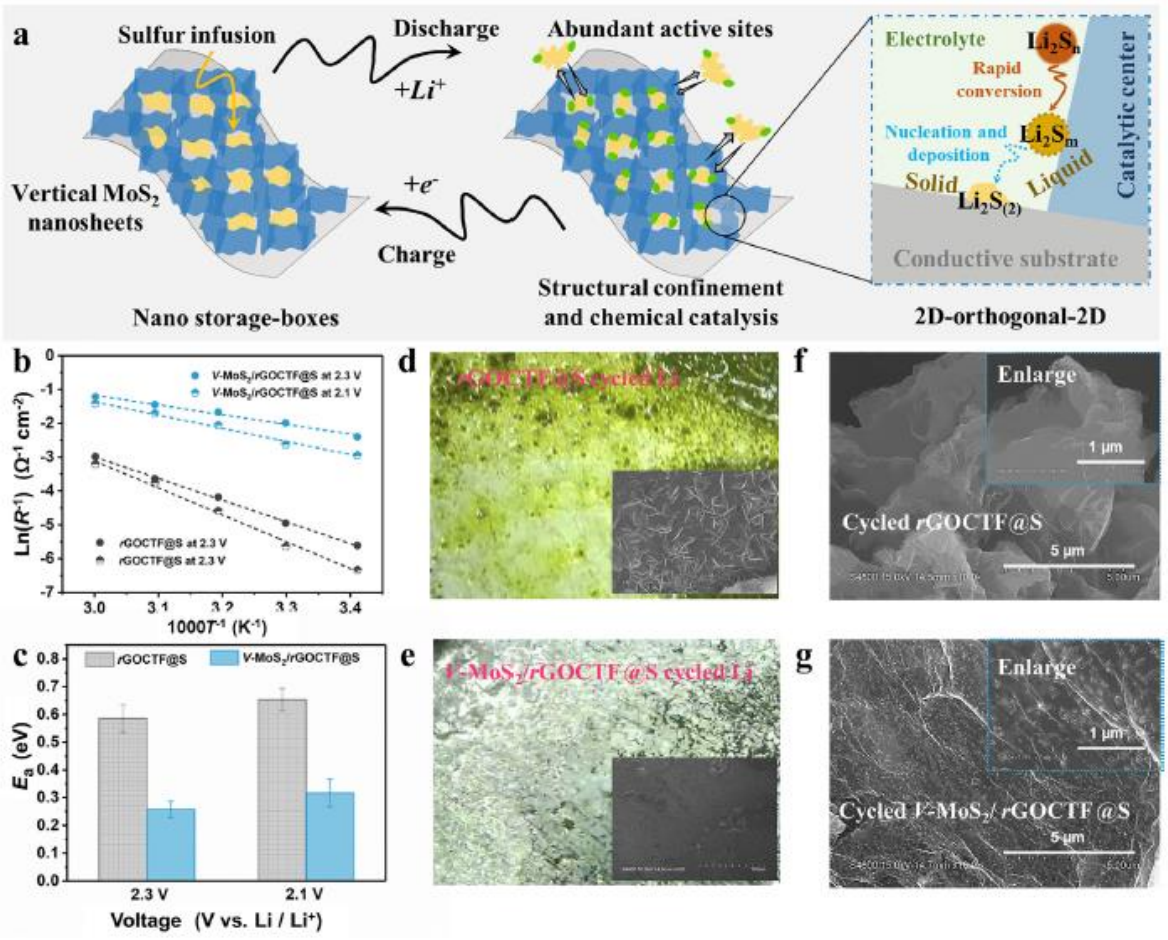

Fig. 5. (a) Study on stabilization mechanisms of V-MoS_2/rGOCTF//LE//Li cell. (b) Charge transfer resistance-temperature curves of rGOCTF//LE//Li and V-MoS_2/rGOCTF//LE//Li cells at various voltages and (c) the corresponding activation energy. Optical microscope images and (inset) FE-SEM images of the lithium anode after cycling using (d) rGOCTF@S and (e) V-MoS_2/rGOCTF@S as cathodes. FE-SEM images of (f) rGOCTF@S and (g) V-MoS_2/rGOCTF@S cathodes, and (inset) the corresponding partial enlarged image under 1.7 V discharge state.

In the nano storage-box, the rGO bottom serves as the conductive substrate, the V-MoS_2 wall serves as the catalytic center, and enough electrolyte is stored in the box. LiPSs rely on the abundant active sites on V-MoS_2 to undergo rapid conversion, and then use the electrolyte in the box as a medium to nucleate and deposit lithium sulfide on the bottom of the box. Abundant catalytic active sites, 2D-orthogonal-2D microstructure confinement, and chemical catalysis with a clear division of labor in the nano storage-box together promote the improvement of the electrochemical performance of the V-MoS_2/rGOCTF@S//LE//Li battery.

Fig. 5(b and c) further explore the catalytic mechanism of the V-MoS_2/rGOCTF@S. The transfer of charge is an important step in the transfer of ions and electrons to the active center to participate in the reaction [**19**]. Therefore, the charge transfer kinetics at the catalyst-adsorption interface is the main factor that determines the kinetics of the electro catalytic reaction. By testing the EIS spectra of discharge potentials for 2.3 and 2.1 V at different temperatures, the dependence of Rct on temperature was determined in **Fig. 5**(b). Among them, 2.3 V corresponds to the conversion of S_8 to

high-order long-chain LiPSs (initial reduction), and 2.1 V corresponds to the conversion of long-chain LiPSs to short-chain LiPSs (median reduction). According to the Arrhenius equation, we have determined the activation energy (E_a) of the rGOCTF@S//LE//Li and the V-MoS_2/rGOCTF@S//LE//Li at different voltages. From the S_8 ring molecule to its diffusion, adsorption, reaction and desorption to form the final discharge products, it is a process that gradually becomes difficult, and the E_a is $E_{a23\ V} < E_{a21\ V}$. With the introduction of V-MoS_2, the activation energy is greatly reduced, which is consistent with the superior electro catalytic kinetics of the V-MoS_2/rGOCTF@S//LE//Li. Interestingly, the acceleration of the V-MoS_2 for the initial reduction and the median reduction is similar, and the E_a decreases by 56% and 51%, respectively. This shows that the electro catalysis of the V-MoS_2 is a synchronously accelerated process for the two-step reduction of lithium-sulfur batteries. The discharge curves of the rGOCTF@S//LE//Li and the V-MoS_2/ rGOCTF@S//LE//Li under different sulfur loadings in **Fig. S17** further support this point of view. It is found that the capacity contribution ratios of the two-step reduction process are all be consistent.

The batteries after 500 cycles were disassembled in the glove box, and the photos of the lithium sheet were captured in the glove box with a WiFi-optical microscope (**Fig. 5**d and e). The rGOCTF@S due to the lack of capture and conversion of LiPSs, a large number of active substances were lost, 'sulfur shuttle' was serious, and yellow viscous liquid was observed on the surface of lithium sheet (**Fig. 5**d). In addition, in the inset, it can be seen that a large number of dendrites are produced on the surface of the lithium sheet and the lithium sheet is severely corroded in the cross-sectional FE-SEM image (**Fig. S18**a). The V-MoS_2/rGOCTF@S//LE//Li benefited from the existence of the nano-catalyst boxes, which bound the active material. The surface and cross-section of the lithium sheet (**Fig. S18**b) were very flat and did not capture the shuttle of LiPSs (**Fig. 5**e). After 500 cycles, it can be seen from the FE-SEM image of the rGOCTF@S cathode under the 1.7 V discharge state that the graphene sheet is bare (**Fig. 5**f), and most of the active materials have been lost, showing low sulfur utilization. On the contrary, a large amount of uniform flake-like lithium sulfide deposition was clearly observed on the V-MoS_2/rGOCTF@S graphene sheet (**Fig. 5**g), which shows that the 2D-orthogonal-2D catalytic nano box ensures high sulfur utilization, improves battery performance, and maintains the integrity of the electrode structure (**Fig. S19**).

4. Conclusions

In summary, the vertical growth of MoS2 on graphene was used to construct nano storage-boxes with V-MoS_2 as the wall and rGO as the bottom. The 2D-orthogonal-2D structure successfully made V-MoS_2 exposed more edge active sites. The active materials are uniformly encapsulated in the nano boxes, and undergo a highspeed and stable oxidation-reduction reaction in the nano reactors. The deposition amount of lithium sulfide on V-MoS_2/rGOCTF is 143 mAh g^{-1}, which is twice that of the rGOCTF. Compared with the rGOCTF@S, the Tafel curve of the V-MoS_2/rGOCTF@S has a lower slope (40 mV dec^{-1}), which means faster reaction kinetics. The synchronous acceleration mechanism of the V-MoS_2/ rGOCTF@S on the two-step reduction reaction of lithium-sulfur batteries ensures its excellent electro catalytic activity. After 500 cycles, uniform lithium sulfide deposition was observed on the V-MoS_2/rGOCTF@S cathode. The presence of nano storage-boxes greatly reduced the loss of active materials and improved the electrochemical performance of the Li-S battery.

References

[1] M. Armand, J.M. Tarascon, Nature 451 (2008) 652-657.

[2] B. Dunn, H. Kamath, J.M. Tarascon, Science 334 (2011) 928-935.

[3] X.L Ji, K.T. Lee, L.F. Nazar, Nat. Mater. 8 (2009) 500-506.

[4] X. Fang, H. Peng, Small 11 (2015) 1488-1511.

[5] S. Urbonaite, T. Poux, P. Novák, Adv. Energy Mater. 5 (2015) 15001181500137.

[6] H.J. Peng, J.Q. Huang, X.B. Cheng, Q. Zhang, Adv. Energy Mater. 7 (2017) 1700260.

[7] X. Liu, J.Q. Huang, Q. Zhang, L.Q. Mai, Adv. Mater. 29 (2017) 1601759.

[8] X. Liu, Y. Li, X. Xu, L Zhou, L.Q. Mai, J. Energy Chem. 61 (2021) 104-134.

[9] L. Hu, C. Dai,J.M. Lim, Y. Chen, X. Lian, M.Wang, Y. Li, P. Xiao, G. Henkelman, M. Xu, Chem. Sci. 9 (2018) 666-675.

[10] Q. Shao, P. Lu, L. Xu, D. Guo, J. Gao, Z.S. Wu, J. Chen, J. Energy Chem. 51 (2020) 262-271.

[11] B. Yu, Y. Chen, Z. Wang, D. Chen, X. Wang, W. Zhang, J. He, W. He, Power Sources 447 (2020) 227364.

[12] E. Cha, M.D. Patel, J. Park, J. Hwang, V. Prasad, K. Cho, W. Choi, Nat. Nanotechnol. 13 (2018) 337-344.

[13] N. Zheng, G. Jiang, X. Chen, J. Mao, N. Jiang, Y. Li, Nano-Micro Lett. 11 (2019)43.

[14] J. Yang, L Yu, B. Zheng, N. Li, J. Xi, X. Qiu, Adv. Sci. 7 (2020) 1903260.

[15] S. Huang, Z. Wang, Y.V. Lim, Y. Wang, Y. Li, D. Zhang, H.Y. Yang, Adv. Energy Mater. 11 (2021) 2003689.

[16] M. Zhao, X. Chen, X.Y. Li, B.Q. Li, J.Q. Huang, Adv. Mater. 33 (2021) 2007298.

[17] P. Wang, B. Xi, M. Huang, W. Chen, J. Feng, S. Xiong, Adv. Energy Mater. 11 (2021) 2002893.

[18] W.P. Wang, J. Zhang, J. Chou, Y.X. Yin, Y. You, S. Xin, Y.G. Guo, Adv. Energy Mater. 11 (2021) 2000791.

[19] L. Peng, Z. Wei, C. Wan, J. Li, Z. Chen, D. Zhu, D. Baumann, H. Liu, C.S. Allen, X. Xu, A.I. Kirkland, I. Shakir, Z. Almutairi, S. Tolbert, B. Dunn, Y. Huang, P. Sautet, X. Duan, Nature Catalysis 3 (2020) 762-770.

[20] A.M. Abraham, S.P. Kammampata, S. Ponnurangam, V. Thangadurai, ACS Appl. Mater. Inter. 11 (2019) 35729-35737.

[21] Y. Yi, Z. Liu, P. Yang, T. Wang, X. Zhao, H. Huang, Y. Cheng, J. Zhang, M. Li, J. Energy Chem. 45 (2020) 18-24.

[22] T. Lei, Y. Xie, X. Wang, S. Miao, J. Xiong, C. Yan, Small 13 (2017) 1701013.

[23] Q. Wu, Z. Yao, X. Zhou, J. Xu, F. Cao, C. Li, ACS Nano 14 (2020) 3365-3377.

[24] Y. Song, W. Zhao, L. Kong, L. Zhang, X. Zhu, Y. Shao, F. Ding, Q. Zhang, J. Sun, Z. Liu, Energy Environ. Sci. 12 (2018) 2620-2630.

[25] T. Guo, Y. Song, Z. Sun, Y. Wu, Y. Xia, Y. Li, J. Sun, K. Jiang, S. Dou, J. Sun,J. Energy Chem. 42 (2020) 34-42.

[26] A.Y.S. Eng, J.L. Cheong, S.S. Lee, Appl. Mater. Today 16 (2019) 529-537.

[27] G. Chen, Y. Li, W. Zhong, F. Zheng, J. Hu, X. Ji, W. Liu, C. Yang, Z. Lin, M. Liu, Energy Stor. Mater. 25 (2020) 547-554.

[28] Y.S. Liu, Y.L Bai, X. Liu, C. Ma, X.Y. Wu, X. Wei, Z. Wang, K.X. Wang, J.S. Chen, Chem. Eng. J. 378 (2019) 122208.

[29] X. Meng, Z. Li, Z. Cheng, P. Li, R. Wang, X. Li, Nanoscale 13 (2021) 5292-5299.

[30] T. Zhou, W. Lv, J. Li, G. Zhou, Y. Zhao, S. Fan, B. Liu, B. Li, F. Kang, Q.H. Yang, Energy Environ. Sci. 10 (2017) 1694-1703.

[31] Y. Chen, W. Zhang, D. Zhou, H. Tian, D. Su, C. Wang, D. Stockdale, F. Kang, B. Li, G. Wang, ACS Nano 13 (2019) 4731-4741.

[32] J. Shen, X. Xu, J. Liu, Z. Liu, F. Li, R. Hu, J. Liu, X. Hou, Y. Feng, Y. Yu, M. Zhu, ACS Nano 13 (2019) 8986-8996.

[33] H. Yuan, X. Chen, G. Zhou, W. Zhang, J. Luo, H. Huang, Y. Gan, C. Liang, Y. Xia, J. Zhang, J. Wang, X. Tao, ACS Energy Lett. 2 (2017) 1711-1719.

[34] S. Ruan, Z. Huang, W. Cai, C. Ma, X. Liu, J. Wang, W. Qiao, L Ling, Chem. Eng. J. 385 (2020) 123839-123850.

[35] Z. Wang, M. Feng, H. Sun, G. Li, Q. Fu, H. Li, J. Liu, L. Sun, A. Mauger, C. Julien, Nano Energy 59 (2019) 390-398.

[36] S. Zhang, P. Zhang, R. Hou, B. Li, Y. Zhang, K. Liu, X. Zhang, G. Shao, Energy Chem 47 (2020) 281-290.

[37] H. Lin, L Yang, X. Jiang, G. Li, T. Zhang, Q. Yao, G.W. Zheng, J.Y. Lee, Energy Environ. Sci 10 (2017) 1476-1486.

[38] W. Yang, W. Yang, L. Dong, X. Gao, G. Wang, G. Shao, J. Mater. Chem. A 7 (2019) 13103-13112.

[39] Z. Yuan, H.J. Peng, T.Z. Hou, J.Q. Huang, C.M. Chen, D.W. Wang, X.B. Cheng, F. Wei, Q. Zhang, Nano Lett. 16 (2016) 519-527.

[40] X. Liu, Q. He, H. Yuan, C. Yan, Y. Zhao, X. Xu, J.Q. Huang, Y.L. Chueh, Q. Zhang, L. Q. Mai, J. Energy Chem. 48 (2020) 109-115.

[41] H. Wang, Q. Zhang, H. Yao, Z. Liang, H. Lee, P. Hsu, G. Zheng, Y. Cui, Nano Lett 14 (2014) 7138-7144.

[42] L. Tan, X.H. Li, Z.X. Wang, H.J. Guo, J.X. Wang, ACS Appl. Mater. Inter. 10 (2018) 3707-3713.

[43] M. Wang, H. Yang, K. Shen, H. Xu, W. Wang, Z. Yang, L. Zhang, J. Chen, Y. Huang, M. Chen, D. Mitlin, X. Li, Small Methodes 4 (2020) 200353.

[44] H. Lin, S. Zhang, T. Zhang, H. Ye, Q. Yao, G.W. Zheng, J.Y. Lee, Adv. Energy Mater. 9 (2019) 1902096.

[45] Z. Cheng, Y. Chen, Y. Yang, L. Zhang, H. Pan, X. Fan, S. Xiang, Z. Zhang, Adv. Energy Mater. 1 (2021) 2003718.

[46] S. Wang, S. Feng, J. Liang, Q. Su, F. Zhao, H. Song, M. Zheng, Q. Sun, Z. Song, X. Jia, J. yang, Y. Li, J. Liao, R. Li, X. Sun, Adv. Energy Mater. 11 (2021) 2003314.

[47] Y. Zhang, Z. Mu, C. Yang, Z. Xu, S. Zhang, X. Zhang, Y. Li, J. Lai, Z. Sun, Y. Yang, Y. Chao, C. Li, X. Ge1, W. Yang, S. Guo, Adv. Funct. Mater. 38 (2018) 1707578.

[48] J. Balach, T. Jaumann, L Giebeler, Energy Storage Materials 8 (2017) 209-216.

[49] H. Jiang, D. Ren, H. Wang, Y. Hu, S. Guo, H. Yuan, P. Hu, L Zhang, C. Li, Adv. Mater. 27 (2015) 3687-3695.

[50] M. Li, H. Peng, Y. Pei, F. Wang, Y. Zhu, R. Shi, X. He, Z. Lei, Z. Liu, J. Sun, Nanoscale 12 (2020) 23636-23644.

[51] J. Ren, Y. Zhou, L Xia, Q. Zheng, J. Liao, E. Long, F. Xie, C. Xu, D. Lin, J. Mater. Chem. A 6 (2018) 13835-13847.

[52] R. Fang, K. Chen, L. Yin, Z. Sun, F. Li, H.M. Cheng, Adv. Mater. 31 (2019) 1800863.

[53] A. Jiménez-Suárez, S.G. Prolongo, Appl. Sci. 10 (2020) 1753.

[54] C. Liu, Y. Bai, Y. Zhao, H. Yao, H. Pang, Energy Stor. Mater. 33 (2020) 470-502.

[55] L. Carbone, A.E. Del Rio Castillo, J. Kumar Panda, G. Pugliese, A. Scarpellini, F. Bonaccorso, V. Pellegrini, ChemSusChem 13 (2020) 1593-1602.

[56] S. Yuan, Z. Guo, L. Wang, S. Hu, Y. Wang, Y. Xia, Adv. Sci. 2 (2015) 1500071.

[57] W. Li, J. Qian, T. Zhao, Y. Ye, Y. Xing, Y. Huang, L. Wei, N. Zhang, N. Chen, L. Li, F. Wu, R. Chen, Chen. Adv. Sci. 6 (2019) 1802362.

[58] J. Guerrero-Contreras, F. Caballero-Briones, Mater. Chem. Phys. 153 (2015) 209-220.

[59] M.W. Marshall, S. Popa-Nita, J.G. Shapter, Carbon 44 (2006) 1137-1141.

[60] J. He, G. Hartmann, M. Lee, G. Hwang, Y. Chen, A. Manthiram, Energy Environ. Sci. 12 (2019) 344-350.

[61] V.V. Korolkov, S.A. Svatek, A. Summerfield, J. Kerfoot, L. Yang, T. Taniguchi, K. Watanabe, N.R. Champness, N.A. Besley, P.H. Beton, ACS Nano 9 (2015) 1034710355.

[62] F. Li, T. Huang, Y. Lan, T. Lu, T. Shen, K. Simbulan, J. Qi, Nanoscale 11 (2019) 13725-13730.

[63] C. Trovatello, H.P.C. Miranda, A. Molina-Sánchez, R. Borrego-Varillas, C. Manzoni, L. Moretti, L. Ganzer, M. Maiuri, J. Wang, D. Dumcenco, A. Kis, L. Wirtz, A. Marini, G. Soavi, A.C. Ferrari, G. Cerullo, D. Sangalli, S.D. Conte, ACS Nano 14 (2020) 5700-5710.

[64] G. Alonso, M.H. Siadati, G. Berhault, A. Aguilar, S. Fuentes, R.R. Chianelli, Appl. Catal. A-Gen. 263 (2004) 109-117.

[65] K. Mahankali, N.K. Thangavel, D. Gopchenko, L.M.R. Arava, ACS Appl. Mater. Inter. 12 (2020) 27112-27121.

[66] C. Wang, L. Sun, K. Li, Z. Wu, F. Zhang, L. Wang, ACS Appl. Mater. Inter. 12 (2020) 43560-43567.